Combination of H-Alpha Decomposition and Migration for Enhancing Subsurface Target Classification of GPR

Xuan Feng, *Member, IEEE*, Yue Yu, Cai Liu, and Michael Fehler

***Abstract*—Polarimetric technology has been one of the most important advances in microwave remote sensing during recent decades. H-alpha decomposition, which is a type of polarimetric analysis technique, has been common for terrain and land-use classification in polarimetric synthetic aperture radar. However, the technique has been less common in the ground penetrating radar (GPR) community. In this paper, we apply the H-alpha decomposition to analyze the surface GPR data to obtain polarimetric attributes for subsurface target classification. Also, by combining H-alpha decomposition and migration, we can obtain a subsurface H-alpha color-coded reconstructed target image, from which we can use both the polarimetric attributes and the geometrical features of the subsurface targets to enhance the ability of subsurface target classification of surface GPR. A 3-D full polarimetric GPR data set was acquired in a laboratory experiment, in which four targets, a scatterer with many branches, a ball, a plate, and a dihedral scatter, were buried in dry sand under flat ground surface, and used to test these techniques. As results, we obtained the subsurface H-alpha distribution and classified the subsurface targets. Also, we derived a subsurface H-alpha color-coded reconstructed target image and identified all four targets in the laboratory experiment.**

***Index Terms*—Classification, ground penetrating radar (GPR), H-alpha decomposition, imaging, migration, subsurface targets.**

I. Introduction

GROUND penetrating radar (GPR) is a type of electromagnetic (EM) technique designed primarily for the detection of objects or interfaces buried beneath the earth's surface or located within a visually opaque structure. The general objective of GPR signal processing, including migration, is to present an image that can readily be interpreted or to distinguish the target [1]. The migration technique, which essentially reconstructs the target reflector surface image from the record data [1], [2], has been well developed in seismic data processing. A number of different migration methodologies, for example, reverse time migration [3]–[5], F-K migration [6], and Kirchhoff migration [7]–[9], have been applied successfully to a range of different GPR applications. Depending on the geometrical features of the subsurface reconstructed image achieved by the migration technique, we can possibly distinguish subsurface targets. However, it is not always easy to identify subsurface targets directly using only the image because different targets may have a similar image.

Other attributes, which may be either directly sensitive to the desired geologic feature or sensitive to the physical property of interest, can help us visually enhance or quantify features of interpretation interest. Recently, attribute analysis methods have begun to be used in GPR prospecting [10]. A number of papers have shown that the methods can be successfully applied to detect different subsurface targets, including soil dielectric permittivity [11], archaeological objects [12], [13], faults [14], fluid [15], [16], and contaminant [17].

Polarization is also a type of useful attribute of an EM wave and can enhance the classification ability. Polarimetric technology has been one of the most important advances in microwave remote sensing during recent decades [18], [19]. Recently, the polarimetric GPR, including polarimetric borehole radar [20]–[22], has been developed, and polarimetric signal analysis has been applied to identify subsurface fractures [20], [21], [23], pipes [24], and unexploded ordnance [25], [26].

The polarimetric decomposition technique, which can extract a polarization attribute, is a type of polarimetric analysis technique. The technique has been common for terrain and land-use classification in polarimetric synthetic aperture radar (SAR) [27]. However, it has been less common in the GPR community. H-alpha decomposition, which is a type of polarimetric decomposition method, is based on the Kennaugh matrix [28]. Two features derived from this decomposition, H, which is a global measure for the distribution of the components of a scattering process, and alpha, which represents a wide variety of different scattering mechanisms, are keys for the application of the method to classification [21], [28].

In this paper, we apply the H-alpha decomposition to surface GPR for subsurface target classification. Combining the

Manuscript received November 8, 2014; revised January 23, 2015; accepted March 3, 2015. This work was supported in part by the 973 Program under Grant 2013CB429805, by the Specialized Research Fund for the Doctoral Program of Higher Education under Grant 20130061110061, by the 863 Program under Grant 2012AA052801, by the National Natural Science Foundation of China under Grant 41430322, and by the Jilin University Seed Foundation for Distinguished Young Scientists. *(Corresponding authors: Xuan Feng and Cai Liu.)*

X. Feng is with the College of Geo-Exploration Science and Technology, Jilin University, Changchun 130026, China, and also with the Earth Resources Laboratory, Department of Earth, Atmospheric and Planetary Sciences, Massachusetts Institute of Technology, Cambridge, MA 02139 USA (e-mail: fengxuan@jlu.edu.cn; xuanfeng@mit.edu).

Y. Yu and C. Liu are with the College of Geo-Exploration Science and Technology, Jilin University, Changchun 130026, China (e-mail: yuyue11@mails.jlu.edu.cn; liucai@jlu.edu.cn).

M. Fehler is with the Earth Resources Laboratory, Department of Earth, Atmospheric and Planetary Sciences, Massachusetts Institute of Technology, Cambridge, MA 02139 USA (e-mail: fehler@mit.edu).

Color versions of one or more of the figures in this paper are available online at http://ieeexplore.ieee.org.

Digital Object Identifier 10.1109/TGRS.2015.2411572

migration technique with the H-alpha decomposition, we also develop a signal processing technique to enhance the subsurface image and improve the classification ability of GPR. We applied the method to 3-D full polarimetric GPR data collected in the laboratory to test the method. All four targets in the laboratory experiment, a scatterer with many branches, a ball, a plate, and a dihedral scatter, were distinguished.

II. Methodology

Because the subsurface target can change the polarization of the scattered wave to be different from the polarization of the incident wave, the receiving antenna of a full polarimetric GPR must be designed to receive the different polarization components of the EM wave. At the same time, to generate EM waves with different polarizations, the transmitting antenna needs to generate signals with components in three orthogonal or basis polarization directions. Therefore, a full set of scattered radar measurements comprise nine components, which are configured by combining three orthogonal (X,Y,Z) transmitting antennas and three orthogonal (X,Y,Z) receiving antennas. However, generally, only antennas in the X-Y plane are really used in GPR surveys. Consequently, the two most common basis polarizations are horizontal linear (H) polarization and vertical linear (V) polarization in the X-Y plane. Therefore, an antenna array of a full polarimetric GPR system using H and V linear polarizations must have four polarimetric modes, HH mode, VV mode, VH mode, and HV mode. Here, in the pair of symbols, the first symbol denotes the polarization of the transmitting antenna, and the second symbol denotes the polarization of the receiving antenna. Because the full polarimetric GPR transmit and receive coordinate systems are identical, the role of the transmitting and the receiving antennas can be interchanged. Hence, the HV mode and VH mode have the same function. Consequently, the full polarimetric GPR system generally uses three polarimetric modes of antenna array and acquires three types of polarimetric GPR data, VV data, HH data, and VH or HV data, at each survey point.

For the polarimetric GPR data, we develop a signal processing technique shown in the Fig. 1. The technique includes mainly three parts, preprocessing, migration and H-alpha decomposition.

A. Preprocessing

The full polarimetric GPR system can be considered to be a stepped frequency radar system. In this case, at each survey point, there are VV, VH, and HH data sets in the frequency domain. For these polarimetric GPR data, the preprocessing procedure includes removing the antenna coupling in the frequency domain, bandpass filtering, inverse fast Fourier transform (IFFT), and subtracting the averaged signal in the time domain.

The procedure of removing the antenna coupling includes two steps. At first, the antenna couplings of three polarimetric modes are measured by pointing the antenna array into the air. Second, the antenna couplings are subtracted from the corresponding polarimetric data in the frequency domain, respectively.

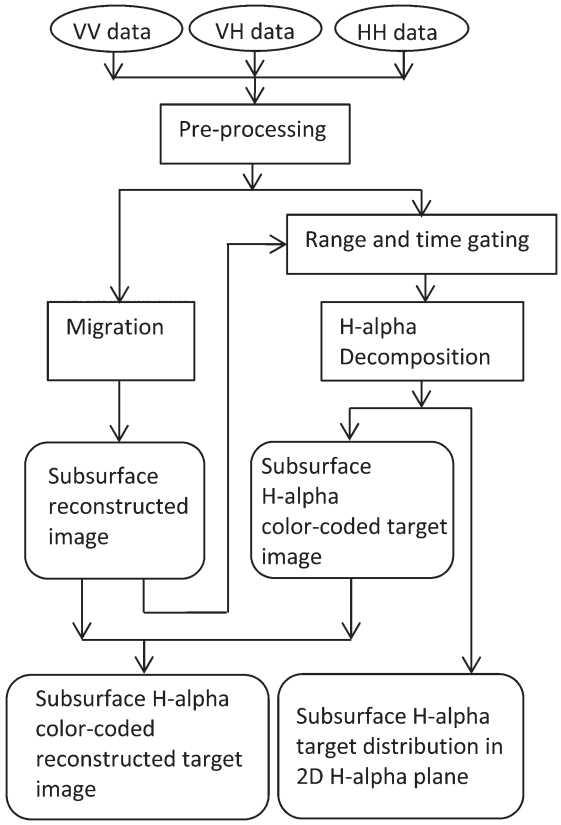

Fig. 1. Processing flowchart to polarimetric GPR data.

Then, the frequency domain data are transformed into the time domain by IFFT. The procedure of subtracting the averaged signal also includes two steps. The first step is that we average each polarimetric data to obtain three averaged signals. The second step is that the averaged signals are subtracted from the corresponding polarimetric data in the time domain, respectively. This processing may suppress strong air/ground reflection signals when the ground surface is almost flat.

B. Migration

The goal of migration is to obtain a reconstructed target image containing its geometrical information in the form of a reflectivity map that shows the locations and geometrical features. Three polarimetric modes of antenna array can be designed to share the same middle point. In this case, the three polarimetric data at each survey point are a type of common midpoint (CMP) data. Therefore, after preprocessing, we have three time domain CMP polarimetric data sets, VV data (S_{vv}), VH data (S_{vh}), and HH data (S_{hh}). For the preprocessed CMP polarimetric data, we use the Kirchhoff prestack migration [2], [7]

$$S_{\text{out}}(x_{\text{out}}, y_{\text{out}}, z) = \frac{1}{2\pi} \iint \frac{\cos\theta}{v_{\text{rms}} r} \frac{\partial}{\partial t} \left[S_{vv}(x, y, t_{vv}) + S_{vh}(x, y, t_{vh}) + S_{hh}(x, y, t_{hh}) \right] dxdy. \quad (1)$$

If three polarimetric modes of the antenna array have the same axis direction and the axis direction is defined as the

$$[T] = \begin{bmatrix} \frac{(S_{hh}+S_{vv})(S_{hh}+S_{vv})^*}{2} & \frac{(S_{hh}-S_{vv})(S_{hh}+S_{vv})^*}{2} & (S_{hh}+S_{vv}){S_{vh}}^* \\ \frac{(S_{hh}-S_{vv})(S_{hh}+S_{vv})^*}{2} & \frac{(S_{hh}-S_{vv})(S_{hh}-S_{vv})^*}{2} & (S_{hh}-S_{vv}){S_{vh}}^* \\ S_{vh}(S_{hh}+S_{vv})^* & S_{vh}(S_{hh}-S_{vv})^* & 2S_{vh}{S_{vh}}^* \end{bmatrix} \tag{3}$$

x-coordinate direction, we can get the travel time of the three modes

$$\begin{aligned} t_{vv} &= \left[\frac{z^2+(x-d_{vv}-x_{\rm out})+(y-y_{out})}{v_{\rm rms}^2}\right]^{\frac{1}{2}} \\ &\quad + \left[\frac{z^2+(x+d_{vv}-x_{\rm out})+(y-y_{\rm out})}{v_{\rm rms}^2}\right]^{\frac{1}{2}} \\ t_{vh} &= \left[\frac{z^2+(x-d_{vh}-x_{\rm out})+(y-y_{\rm out})}{v_{\rm rms}^2}\right]^{\frac{1}{2}} \\ &\quad + \left[\frac{z^2+(x+d_{vh}-x_{\rm out})+(y-y_{\rm out})}{v_{\rm rms}^2}\right]^{\frac{1}{2}} \\ t_{hh} &= \left[\frac{z^2+(x-d_{hh}-x_{\rm out})+(y-y_{\rm out})}{v_{\rm rms}^2}\right]^{\frac{1}{2}} \\ &\quad + \left[\frac{z^2+(x+d_{hh}-x_{\rm out})+(y-y_{\rm out})}{v_{\rm rms}^2}\right]^{\frac{1}{2}}. \end{aligned} \tag{2}$$

In (2), d_{vv} and d_{hh} are the half transmitting antenna-receiving antenna offsets in VV and HH modes, respectively, and d_{vh} is the half transmitting antenna-receiving antenna offset in VH mode. $v_{\rm rms}$ is the root mean square (RMS) velocity above the scatter point $(x_{\rm out}, y_{\rm out}, z)$, and r is the distance between the measurement point $(x, y, 0)$ and the scatter point. In (1), θ is the angle between the direction of propagation and the vertical axis z, and $\cos\theta$ is the obliquity factor or directivity factor describing the angle dependence of amplitude.

After migration, we can have a subsurface reconstructed image showing the geometrical features of subsurface targets. The geometrical features offer us a possible way to identify the subsurface targets. However, if different targets show similar geometrical features in the image, it will be difficult to distinguish them.

C. H-Alpha Decomposition

The geometrical information shown in the migrated image also includes position information for the subsurface targets. Depending on the position information, we can extract signals scattered from the target by the method of range and time gating from the three preprocessed polarimetric data sets. Then, the polarimetric decomposition technique, H-alpha decomposition, is applied to the extracted signals.

The coherency matrix can be parameterized in the form shown in (3) [28], shown at the top of the page. A parameterization of the coherency matrix can be obtained in the form [28]

$$[T] = [U_3][\Lambda][U_3]^{-1} = [U_3]\begin{bmatrix} \lambda_1 & 0 & 0 \\ 0 & \lambda_2 & 0 \\ 0 & 0 & \lambda_3 \end{bmatrix}[U_3]^{-1} \tag{4}$$

where

$$\begin{aligned} [U_3] &= [e_1 \quad e_2 \quad e_3]^T \\ &= \begin{bmatrix} \cos\alpha_1 & \cos\alpha_2 & \cos\alpha_3 \\ \sin\alpha_1\cos\beta_1 e^{j\delta_1} & \sin\alpha_2\cos\beta_2 e^{j\delta_2} & \sin\alpha_3\cos\beta_3 e^{j\delta_3} \\ \sin\alpha_1\cos\beta_1 e^{j\gamma_1} & \sin\alpha_2\cos\beta_2 e^{j\gamma_2} & \sin\alpha_3\cos\beta_3 e^{j\gamma_3} \end{bmatrix} \end{aligned} \tag{5}$$

and where $[\Lambda]$ is the diagonal eigenvalue matrix of $[T]$ with $\lambda_1 \geq \lambda_2 \geq \lambda_3 \geq 0$, and $[U_3]$ is a unitary matrix whose elements correspond to the orthonormal eigenvectors e_1, e_2, and e_3 of the coherency matrix $[T]$. The parameterization of a 3×3 unitary U_3 matrix in terms of column vectors with different parameters α, β, δ, and γ, which are the parameters of the dominant scattering mechanism, is made so as to enable a probabilistic interpretation of the scattering process. The three parameters β, δ, and γ remain rotationally variant [27]. The entropy is defined from the eigenvalues as [28]

$$H = \sum_{i=1}^{3} -P_i \log_3 P_i \tag{6}$$

where

$$P_i = \frac{\lambda_i}{\lambda_1+\lambda_2+\lambda_3}. \tag{7}$$

The parameter $\alpha_{\rm i}$ is associated with a random sequence. The best estimate of the parameter is given by the mean of this sequence which is easily evaluated as [28]

$$\overline{\alpha} = \sum_{i=1}^{3} P_i\alpha_i. \tag{8}$$

Consequently, we can obtain a pair of H-alpha values from each coherency matrix. Then, a 2-D H-alpha classification space, which shows the classical H-alpha plane for random media scattering problems as described by Cloude and Pottier [27], [28] (shown in Fig. 2), is considered. The H-alpha plane is divided into nine basic zones, and the different zones correspond to different physical scattering characteristics [27], [28]. The location of the boundaries within the feasible combinations of H and alpha values is set based on the general properties of the scattering mechanisms. The key idea is that entropy arises as a natural measure of the inherent reversibility of the scattering data and that the alpha can be used to identify the underlying average scattering mechanisms. There is some degree of arbitrariness on the setting of these boundaries which are not dependent on a particular data set [27]. Therefore, we can achieve an H-alpha target distribution in the 2-D H-alpha plane, which can be used to interpret the scattering mechanism of the subsurface target and to classify the subsurface targets.

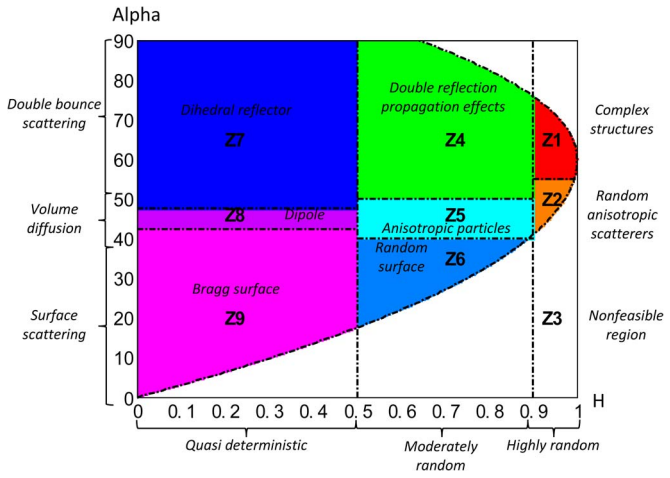

Fig. 2. H-alpha plane for random media scattering problems.

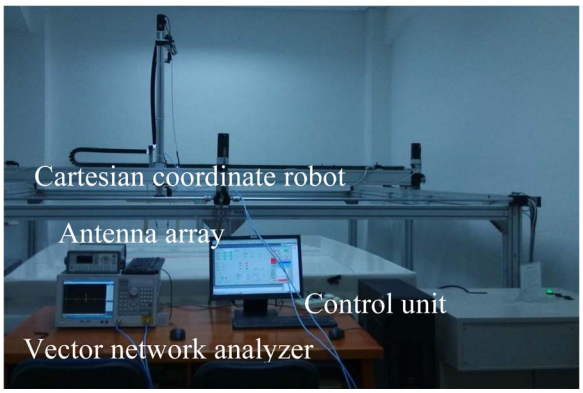

Fig. 3. Full polarimetric GPR system.

D. Subsurface H-Alpha Color-Coded Reconstructed Image

In the H-alpha plane, the eight basic zones can be represented by eight colors shown in Fig. 2 separately. We did not define a color for Zone 3 because it is a nonfeasible region and we cannot distinguish surface scattering with high entropy [27], [28]. Therefore, the colors can show characteristic classes of different scattering behavior. Consequently, each pair of H-alpha values can be represented by a color, and we can achieve a subsurface H-alpha color-coded target image, which can also be used to classify the targets.

Finally, we can combine the H-alpha color-coded target image with the reconstructed image by painting the color determined by the pair of H-alpha values on the reconstructed migration image to result in a subsurface H-alpha color-coded reconstructed image. From the enhanced image, we can obtain the information about not only the geometrical features but also the polarimetric attributes of targets. This information enhances the classification ability of GPR for subsurface targets.

III. Application to Experiment Data

A. Full Polarimetric GPR System and Experiment Setting

A full polarimetric stepped frequency GPR system shown in Fig. 3 consists of a vector network analyzer, a Cartesian coordinate robot, an antenna array, and a control unit (computer).

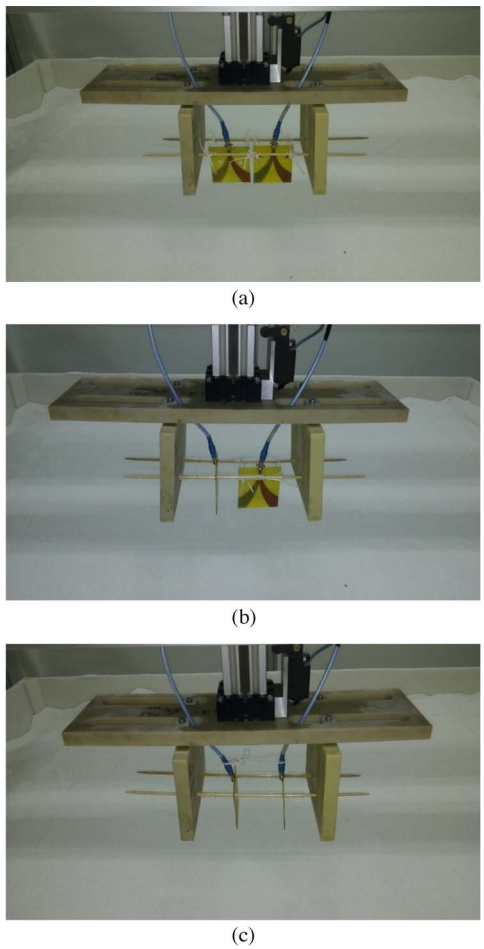

Fig. 4. Polarimetric antenna array. Three polarimetric modes of antenna array are shown. (a) HH mode. (b) VH mode. (c) VV mode.

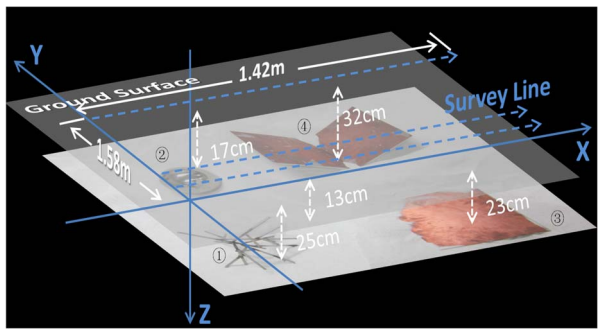

Fig. 5. Experiment setting. Target ① is a metallic scatterer with many branches. Target ② is a metallic ball. Target ③ is a metallic plate. Target ④ is a metallic dihedral scatter.

The network analyzer is an Agilent E5071C whose frequency band is 9 kHz–8.5 GHz. The Cartesian coordinate robot can accurately move the antenna array along a 3-D axis. The antenna array uses a type of Vivaldi antenna [29], [30] and has three types of polarimetric modes, HH mode, VH mode, and VV mode, shown in Fig. 4. It can acquire three types of polarimetric GPR data sets of HH, VH, and VV at each survey point, respectively. The distance between feeding points of transmitting and receiving antennas is 8 cm for all three polarimetric modes with the same axis direction.

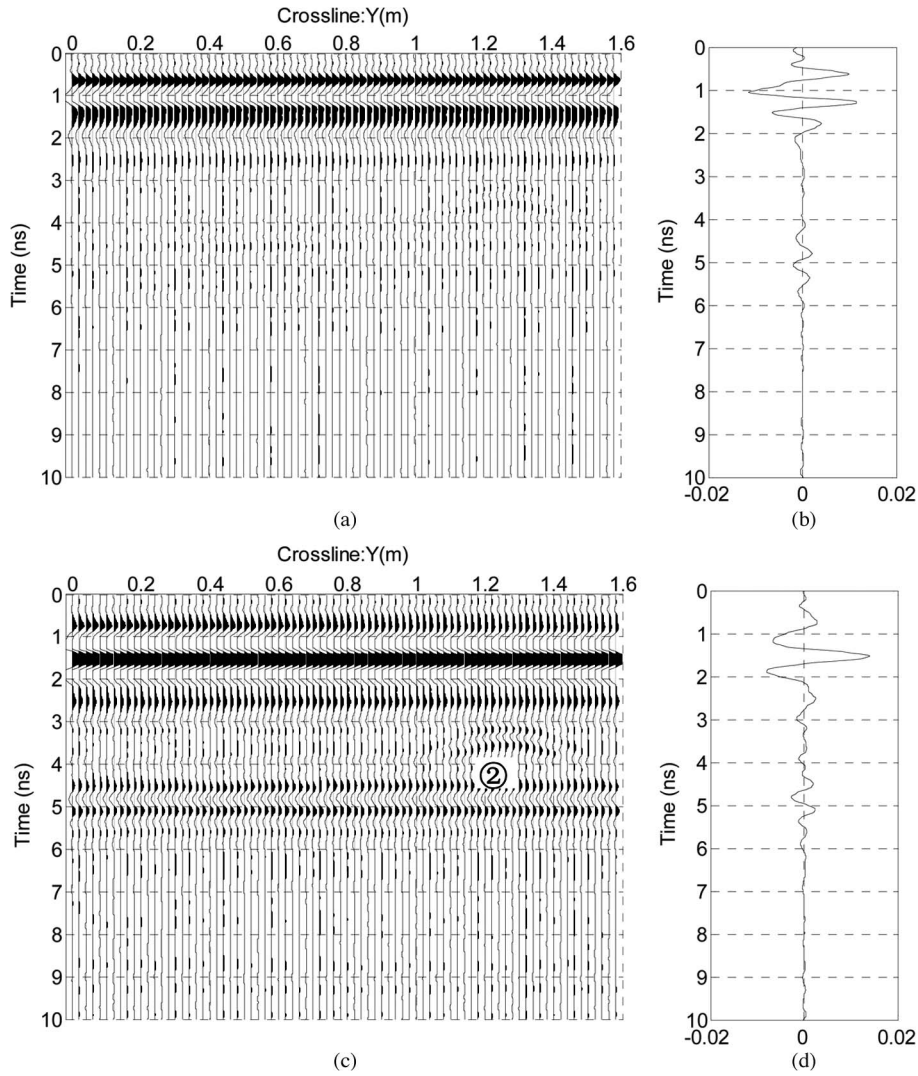

Fig. 6. Cross-line profiles and averaged signal of HH polarimetric data and HH antenna coupling. ② marks the signals from the metallic ball. (a) Raw cross-line profile at $x = 0.4$ m. (b) Antenna coupling. (c) Cross-line profile after removing antenna coupling at $x = 0.4$ m. (d) Averaged signal.

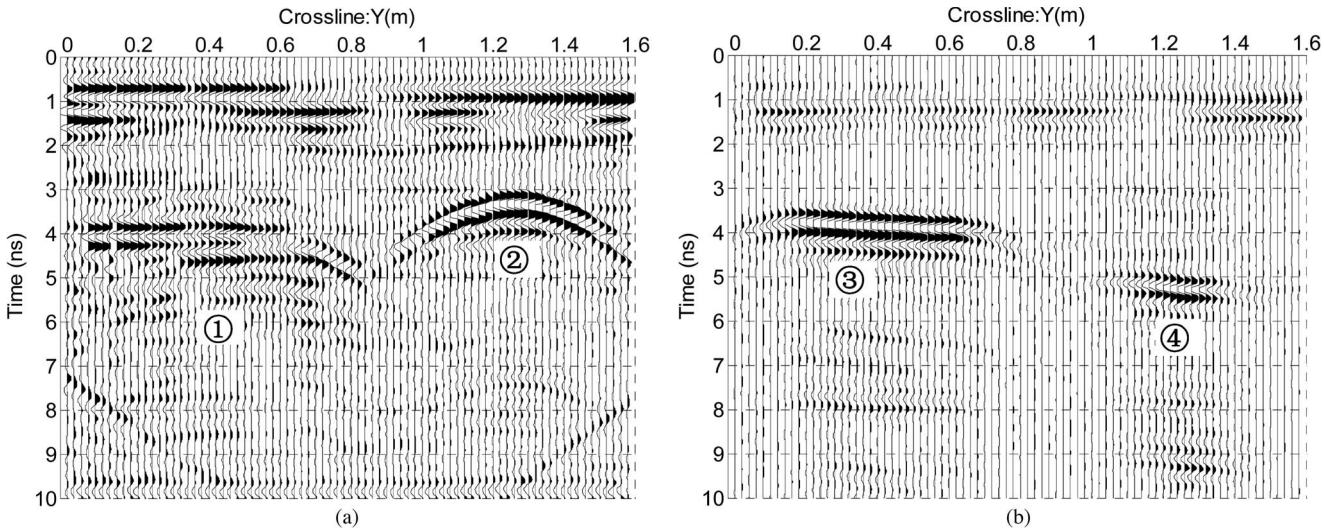

Fig. 7. Preprocessed cross-line profiles of HH polarimetric data. ① marks the signals from the metallic scatterer with many branches. ② marks the signals from the metallic ball. ③ marks signals from the metallic plate. ④ marks signals from the metallic dihedral scatter. (a) Cross-line profile at $x = 0.4$ m. (b) Cross-line profile at $x = 1.0$ m.

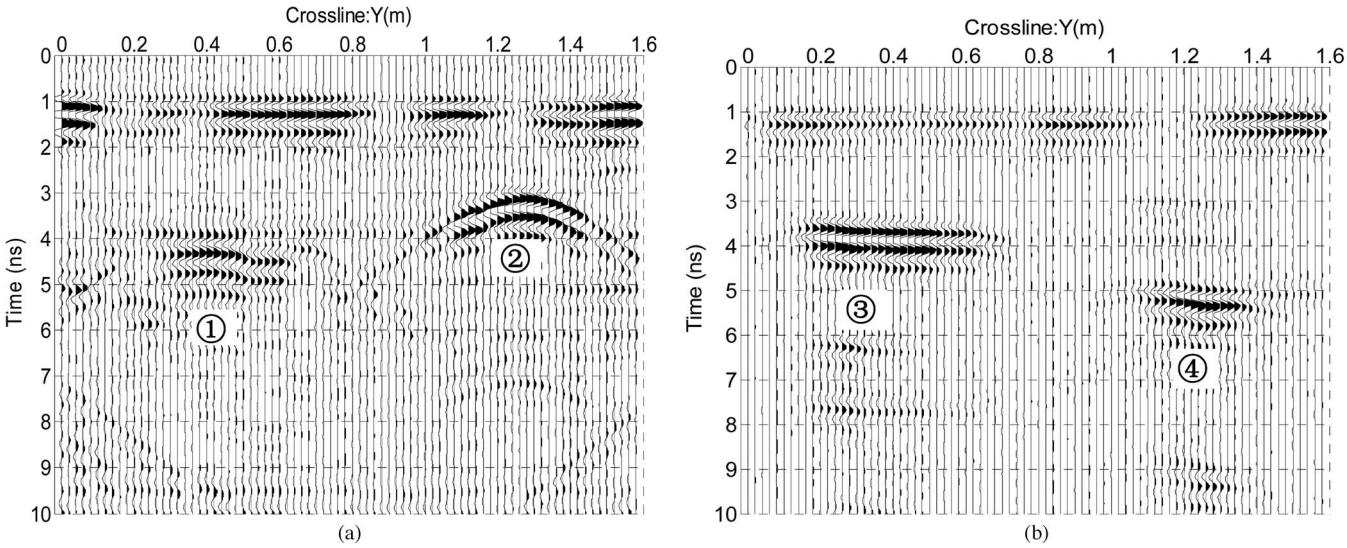

Fig. 8. Preprocessed cross-line profiles of VV polarimetric data. ① marks the signals from the metallic scatterer with many branches. ② marks the signals from the metallic ball. ③ marks signals from the metallic plate. ④ marks signals from the metallic dihedral scatter. (a) Cross-line profile at $x = 0.4$ m. (b) Cross-line profile at $x = 1.0$ m.

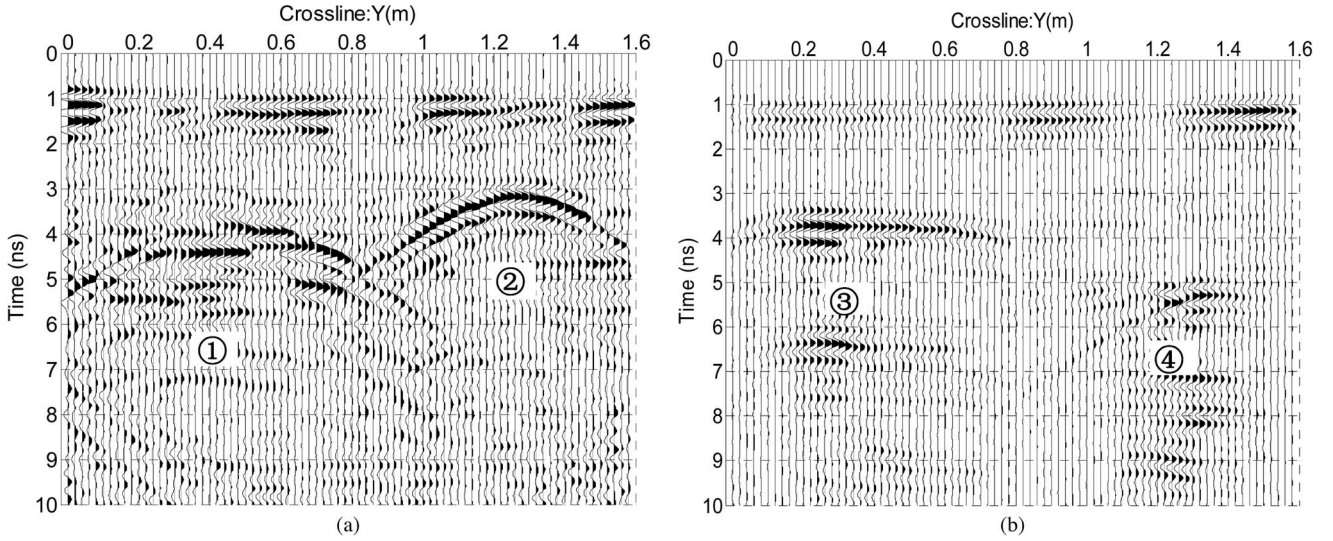

Fig. 9. Preprocessed cross-line profiles of VH polarimetric data. ① marks the signals from the metallic scatterer with many branches. ② marks the signals from the metallic ball. ③ marks signals from the metallic plate. ④ marks signals from the metallic dihedral scatter. (a) Cross-line profile at $x = 0.4$ m. (b) Cross-line profile at $x = 1.0$ m.

Fig. 5 shows the experiment setting. Four targets were buried in homogeneous dry sand. Target ① was a metallic scatterer with many branches buried at a depth of about 25 cm. Target ② was a metallic ball buried at a depth of about 17 cm. Target ③ was a metallic plate buried at a depth of about 23 cm. Target ④ was a metallic dihedral scatter buried at a depth of 32 cm. The ground surface is almost flat.

We carried out a 2-D scanning survey in the experiment. The antenna array was moved at an elevation of 13 cm above the sand. The 2-D scan measurement consists of 80 survey lines with a line interval of 2 cm. The orientation of the survey line is the same as the axis direction of the antenna array. Each survey line consists of 72 measurement points, whose interval is also 2 cm. The frequency used in the experiment ranges between 500 MHz and 4.5 GHz, using 401 equally spaced samples. There are three types of polarimetric antenna collecting data at each survey point, respectively. Consequently, there are three types of data profiles for each survey line. Therefore, the experiment resulted in three 3-D frequency domain data sets, one for each polarimetric mode. Following the technology used in seismic acquisition, we call a set of data along a survey line an in-line profile. Data collected across the survey line are called a cross-line profile.

B. Preprocessing

The preprocessing procedures were used to process the three 3-D data sets. Fig. 6 show an example of the preprocessing.

Fig. 6(a) shows a raw cross-line profile of HH polarimetric data in the time domain at $x = 0.4$ m, and Fig. 6(b) shows the HH antenna coupling in the time domain. Because strong antenna coupling masks the scattering signal from targets, we cannot find target signals in Fig. 6(a). After removing the antenna coupling, the cross-line profile is shown in Fig. 6(c), in which we can find unclear signals from the metallic ball. Then, we average the data to obtain the averaged HH signal shown in Fig. 6(d). After subtracting the averaged signal from the data, we obtain the preprocessed data sets. Figs. 7–9 show the preprocessed data for two lines collected using the HH, VV, and VH modes, respectively. After antenna coupling was removed and ground surface reflection was suppressed by the preprocessing procedures, signals from subsurface targets are clear. In these figures, ① marks the signals from the metallic scatterer with many branches, ② marks the signals from the metallic ball, ③ marks signals from the metallic plate, and ④ marks signals from the metallic dihedral scatter. Figs. 7 and 8 are obtained in the HH and VV modes, respectively, which are the copolarimetric modes that are common in the commercial GPR system. From Figs. 7 and 8, we can find that signals collected over ③ and ④ have similar geometrical features, including horizontal events. Therefore, it is difficult to distinguish between ③ and ④ only from the geometrical characteristics at the data.

C. Migration

Because the gap between transmitting and receiving antenna feeding points is the same in the three polarimetric modes, the acquired data sets are the type of common offset data sets. Therefore, in the case, we have $d_{vv} = d_{vh} = d_{hh}$ and $t_{vv} = t_{vh} = t_{hh}$ in (2).

Because the targets were buried at different depths, a continuous subsurface RMS (C-RMS) velocity model was used here. The C-RMS velocity is given by

$$v_{\mathrm{rms}}(t) = \sqrt{\frac{v_{\mathrm{soil}}^2(t - t_{\mathrm{air}}) + v_{\mathrm{air}}^2 t_{\mathrm{air}}}{t}} \tag{9}$$

where v_{soil} is the propagation velocity in the soil, v_{air} is the velocity in air, and t_{air} is the travel time in air that can be estimated by v_{air} and the height of the antennas.

After the prestack migration, we get a 3-D migrated image for the polarimetric GPR data sets, and the result is shown in Fig. 10. In this figure, the reconstructed 3-D subsurface image is displayed by the method of plotting isosurface, which is a surface that represents points of a constant amplitude value within the volume of 3-D migrated data, in Fig. 10(a). Fig. 10(b) and (c) shows vertical profiles for two lines. From these figures, we can get some geometrical information about the position and size of the subsurface targets. We can distinguish between ② and ③ because the image feature of target ② is circular in the 3-D image and curved event in the vertical profile while the character of target ③ is flat in both the 3-D image and the vertical profile. However, it is still difficult to distinguish between ③ and ④ because their characters are both flat in the 3-D image and the vertical profile.

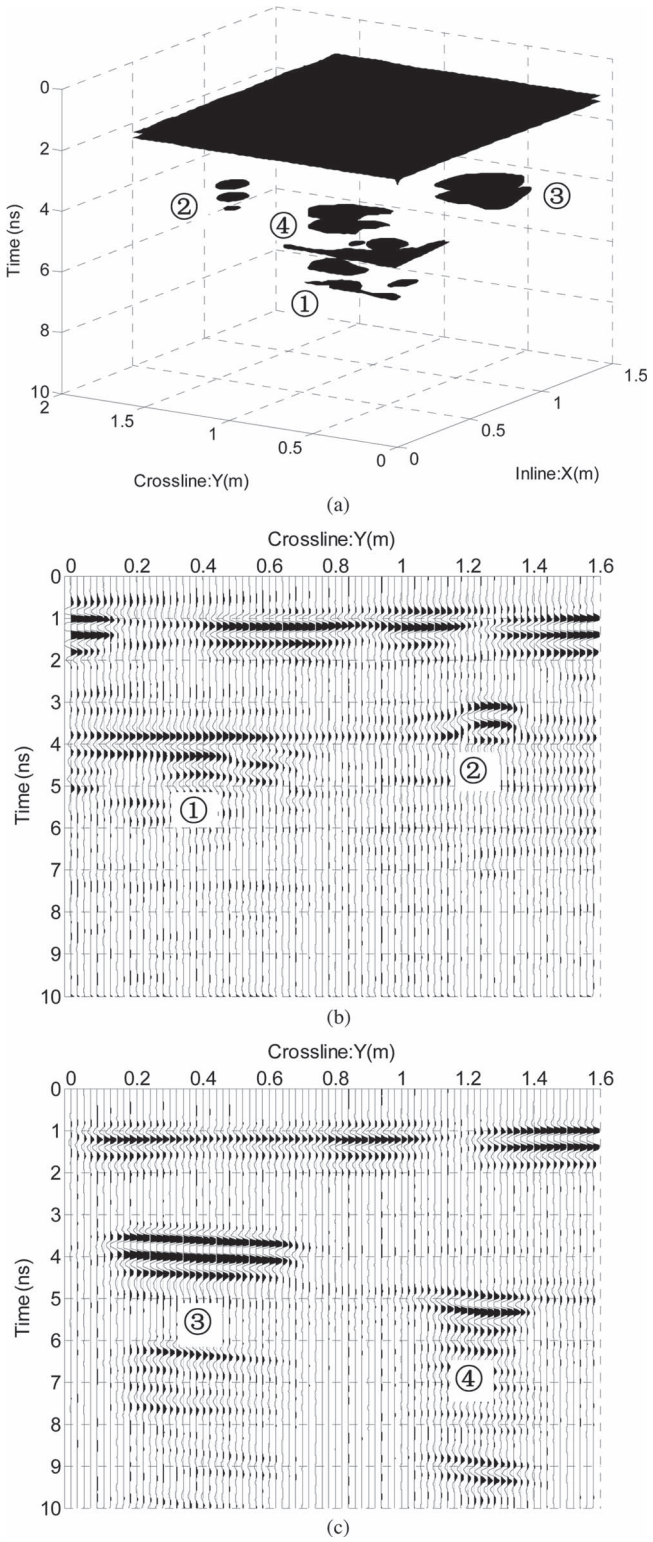

Fig. 10. Migrated data. ① marks the signals from the metallic scatterer with many branches. ② marks the signals from the metallic ball. ③ marks signals from the metallic plate. ④ marks signals from the metallic dihedral scatter. (a) is an isosurface view of the migrated image; (b) and (c) show the vertical cross section of the image. (a) Three-dimensional subsurface reconstructed image. (b) Cross-line profile at $x = 0.4$ m. (c) Cross-line profile at $x = 1.0$ m.

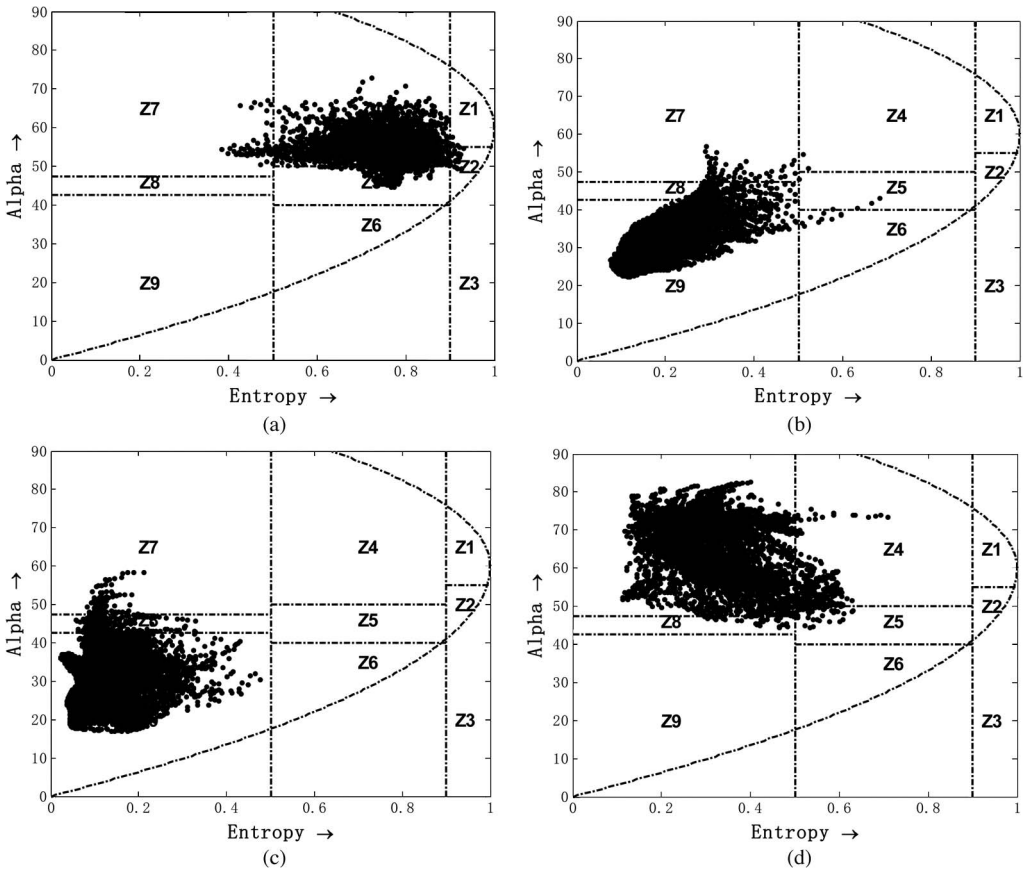

Fig. 11. H-alpha target distribution. Target ① is the metallic scatterer with many branches. Target ② is the metallic ball. Target ③ is the metallic plate. Target ④ is the metallic dihedral scatter. (a) Target ①. (b) Target ②. (c) Target ③. (d) Target ④.

D. Application of H-Alpha Decomposition to Subsurface Targets

From the migrated data (see Fig. 10), we can get position information for the subsurface targets. Depending on the position information, we can extract signals scattered by the four subsurface targets using the method of range and time gating from the three preprocessed polarimetric data sets. Consequently, for each target, we have three selected 3-D polarimetric data sets. The H-alpha decomposition technique is applied to analyze the selected signals of each target, respectively, and the entropy and alpha are computed. Then, the values of H and alpha were projected into the classical H-alpha classification space [28], whose area was divided into nine zones, as shown in Fig. 11.

From Fig. 11(a), we find that most H-alpha values for target ① occur in Zone 4 corresponding to medium entropy multiple scattering, such as forested regions in SAR images [28]. In Fig. 11(b) and (c), we can find that most H-alpha values of targets ② and ③ are found in Zone 9 corresponding to low entropy surface scatter, such as a smooth surface in a SAR image [28]. This coincides with targets ② and ③ being the ball or plate, respectively, in the experiment. In Fig. 11(d), most H-alpha values of target ④ occur in Zone 7, which corresponds to low entropy multiple scattering events, such as metallic dihedral scatter. Consequently, we can distinguish targets ① and ④ in the experiment, but it is difficult to distinguish between targets ② and ③.

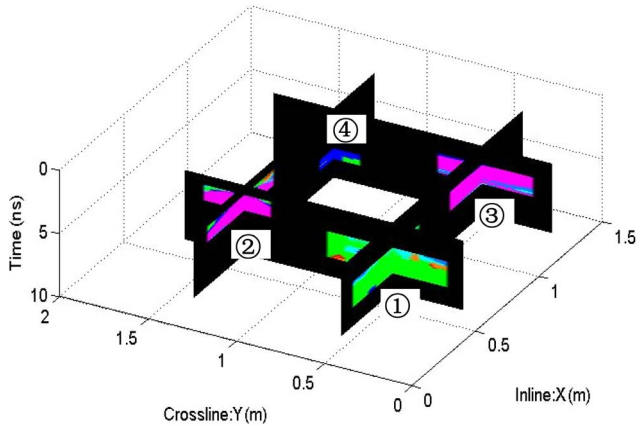

Fig. 12. Subsurface H-alpha color-coded target image. ① marks the result from the metallic scatterer with many branches. ② marks the result from the metallic ball. ③ marks the result from the metallic plate. ④ marks the result from the metallic dihedral scatter.

E. Subsurface H-Alpha Color-Coded Reconstructed Target Image

We can use nine colors to represent the nine zones, respectively, as shown in Fig. 2. For example

Zone $4 \rightarrow$ Green
Zone $7 \rightarrow$ Blue
Zone $9 \rightarrow$ Pink.

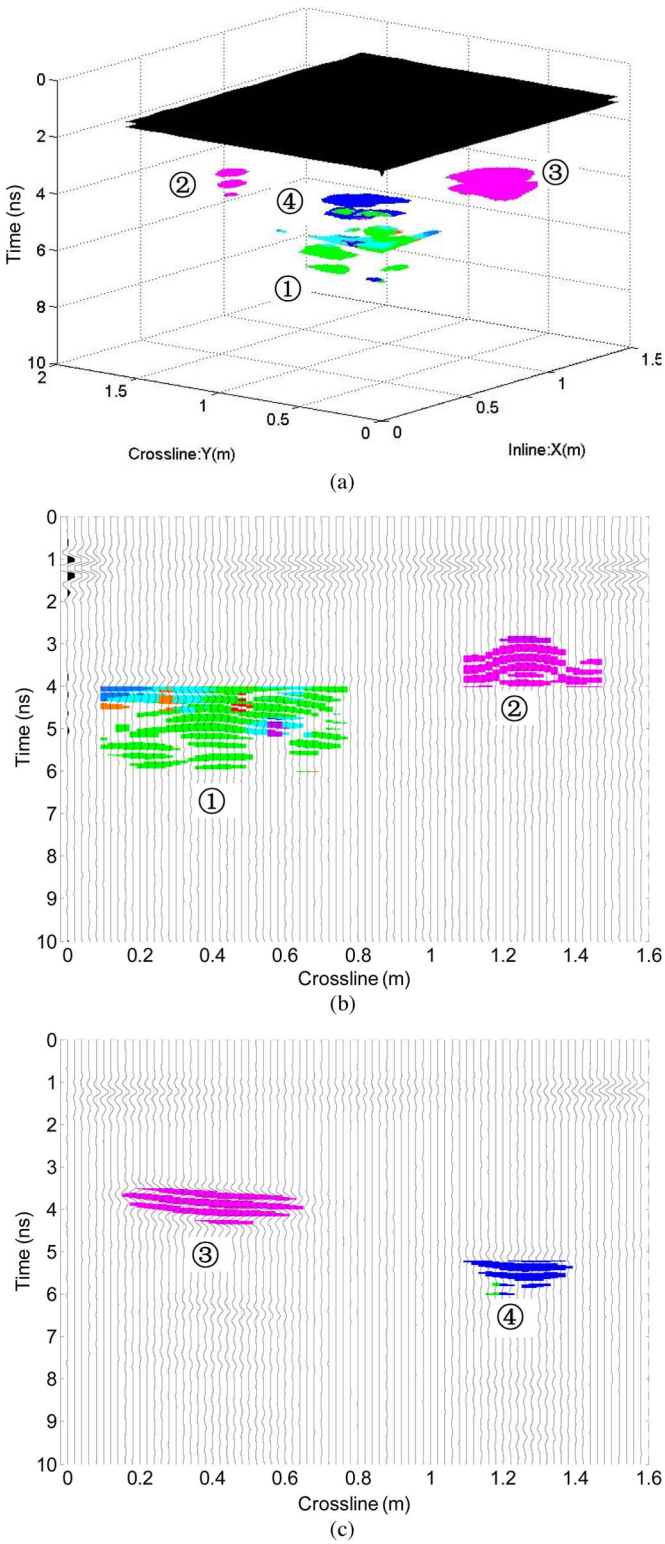

Fig. 13. Subsurface H-alpha color-coded reconstructed target image. ① marks the result from the metallic scatterer with many branches. ② marks the result from the metallic ball. ③ marks result from the metallic plate. ④ marks result from the metallic dihedral scatter. (a) Three-dimensional subsurface H-alpha color-coded reconstructed target image. (b) Cross-line profile at $x = 0.4$ m. (c) Cross-line profile at $x = 1.0$ m.

This means that, if the H-alpha values are projected into Zone 4, the position will be filled with a green color and so on. Then, we can achieve the subsurface H-alpha color-coded target image shown in Fig. 12. The main color of target ① is green, which represents Zone 4. The main color of targets ② and ③ is pink, which corresponds to Zone 9. The main color of target ④ is blue, which refers to Zone 7. From the results of the subsurface H-alpha color-coded target image, we can also classify the four targets into three groups. However, it is still not possible to distinguish between targets ② and ③.

Finally, we can combine the subsurface H-alpha color-coded target image shown in Fig. 12 with the subsurface reconstructed image, which is the result of migration shown in Fig. 10. We paint the color obtained from the subsurface H-alpha color-coded target image on the subsurface reconstructed image and achieve a subsurface H-alpha color-coded reconstructed image shown in Fig. 13.

Fig. 13(a) is the 3-D subsurface H-alpha color-coded reconstructed target image, and Fig. 13(b) and (c) are vertical profiles for two cross-lines of the 3-D image. From these figures, depending on the geometrical features and colors of targets, we can distinguish all four targets. Target ① has a curved event feature and green color, which is the scatterer with many branches in the experiment. Target ② has a curved event feature and pink color, which is the ball in the experiment. Target ③ has a flat event feature and pink color, which is the plate in the experiment. Target ④ has a flat event feature and blue color, which is the dihedral scatter in the experiment.

IV. Conclusion

A type of polarimetric decomposition, H-alpha decomposition, was applied to analyze surface GPR data, which are acquired in homogeneous soil under flat ground surface. H-alpha target distribution and H-alpha color-coded target images were obtained, from which we can analyze polarimetric attributes, classify subsurface targets, and identify some of them. Migration can obtain geometrical features about subsurface targets, from which we can possibly distinguish the characteristics of subsurface targets and identify some targets.

By combining H-alpha decomposition and migration, we can obtain a subsurface H-alpha color-coded reconstructed target image, from which we can use both the polarimetric attributes and the geometrical features of subsurface targets to enhance the ability of subsurface target classification of surface GPR.

References

[1] D. J. Daniels, *Ground Penetrating Radar*, 2nd ed. London, U.K.: Inst. Elect. Eng., 2004.
[2] Ö. Yilmaz and S. M. Doherty, *Seismic Data Analysis: Processing, Inversion, and Interpretation of Seismic Data*, 2nd ed. Tulsa, OK, USA: Soc. Exploration Geophys., 2001.
[3] E. Fisher, G. A. Mcmechan, A. P. Annan, and S. W. Cosway, "Examples of reverse-time migration of single-channel, ground-penetrating radar profiles," *Geophysics*, vol. 57, no. 4, pp. 577–586, Apr. 1992.
[4] C. J. Leuschen and R. G. Plumb, "A matched-filter-based reverse-time migration algorithm for ground-penetrating radar data," *IEEE Trans. Geosci. Remote Sens.*, vol. 39, no. 5, pp. 929–936, May 2001.
[5] H. Zhou, M. Sato, and H. J. Liu, "Migration velocity analysis and prestack migration of common-transmitter GPR data," *IEEE Trans. Geosci. Remote Sens.*, vol. 43, no. 1, pp. 86–91, Jan. 2005.
[6] H. Hayakawa and A. Kawanaka, "Radar imaging of underground pipes by automated estimation of velocity distribution versus depth," *J. Appl. Geophys.*, vol. 40, no. 1–3, pp. 37–48, Oct. 1998.

[7] X. Feng and M. Sato, "Pre-stack migration applied to GPR for landmine detection," *Inv. Probl.*, vol. 20, no. 6, pp. S99–S115, Dec. 2004.
[8] X. Feng, M. Sato, and C. Liu, "Hand-held GPR imaging using migration for irregular data," *IEEE J. Sel. Topics Appl. Earth Observ. Remote Sens.*, vol. 4, no. 4, pp. 799–803, Dec. 2011.
[9] M. L. Moran, R. J. Greenfield, S. A. Arcone, and A. J. Delaney, "Multidimensional GPR array processing using Kirchhoff migration," *J. Appl. Geophys.*, vol. 43, no. 2–4, pp. 281–295, Mar. 2000.
[10] H. M. Jol, *Ground Penetrating Radar: Theory and Applications*, 1st ed. Amsterdam, Netherlands: Elsevier, 2009.
[11] A. Di Matteo, E. Pettinelli, and E. Slob, "Early-time GPR signal attributes to estimate soil dielectric permittivity: A theoretical study," *IEEE Trans. Geosci. Remote Sens.*, vol. 51, no. 3, pp. 1643–1654, Mar. 2013.
[12] U. Böniger, "Improving the interpretability of 3D GPR data using target-specific attributes: Application to tomb detection," *J. Archaeological Sci.*, vol. 37, no. 4, pp. 672–679, 2010.
[13] W. K. Zhao, E. Forte, M. Pipan, and G. Tian, "Ground Penetrating Radar (GPR) attribute analysis for archaeological prospection," *J. Appl. Geophys.*, vol. 97, pp. 107–117, Oct. 2013.
[14] A. F. McClymont *et al.*, "Visualization of active faults using geometric attributes of 3D GPR data: An example from the Alpine Fault Zone, New Zealand," *Geophysics*, vol. 73, no. 2, pp. B11–B23, 2008.
[15] R. M. Corbeanu, G. A. McMechan, R. B. Szerbiak, and K. Soegaard, "Prediction of 3-D fluid permeability and mudstone distributions from ground-penetrating radar (GPR) attributes: Example from the cretaceous ferron sandstone member, East-Central Utah," *Geophysics*, vol. 67, no. 5, pp. 1495–1504, 2002.
[16] B. Schmalz, B. Lennartz, and D. Wachsmuth, "Analyses of soil water content variations and GPR attribute distributions," *J. Hydrol.*, vol. 267, no. 3/4, pp. 217–226, Oct. 2002.
[17] N. J. Cassidy, "Evaluating LNAPL contamination using GPR signal attenuation analysis and dielectric property measurements: Practical implications for hydrological studies," *J. Contaminant Hydrol.*, vol. 94, no. 1–2, pp. 49–75, Oct. 30, 2007.
[18] S. R. Cloude, *Polarisation: Applications in Remote Sensing*, 1st ed. New York, NY, USA: Oxford Univ. Press, 2010.
[19] Y.-Q. Jin and F. Xu, *Polarimetric Scattering and SAR Information Retrieval*, 1st ed. Singapore: Wiley, 2013.
[20] T. Miwa, M. Sato, and H. Niitsuma, "Subsurface fracture measurement with polarimetric borehole radar," *IEEE Trans. Geosci. Remote Sens.*, vol. 37, no. 2, pp. 828–837, Mar. 1999.
[21] J. G. Zhao and M. Sato, "Radar polarimetry analysis applied to single-hole fully polarimetric borehole radar," *IEEE Trans. Geosci. Remote Sens.*, vol. 44, no. 12, pp. 3547–3554, Dec. 2006.
[22] X. Feng *et al.*, "Calibration with high-order terms of polarimetric GPR," *IEEE J. Sel. Topics Appl. Earth Observ. Remote Sens.*, vol. 5, no. 3, pp. 717–722, Jun. 2012.
[23] D. S. Sassen and M. E. Everett, "3D polarimetric GPR coherency attributes and full-waveform inversion of transmission data for characterizing fractured rock," *Geophysics*, vol. 74, no. 3, pp. J23–J34, 2009.
[24] U. Boniger and J. Tronicke, "Subsurface utility extraction and characterization: Combining GPR symmetry and polarization attributes," *IEEE Trans. Geosci. Remote Sens.*, vol. 50, no. 3, pp. 736–746, Mar. 2012.
[25] C. C. Chen, M. B. Higgins, K. O'Neill, and R. Detsch, "Ultrawide-bandwidth fully-polarimetric ground penetrating radar classification of subsurface unexploded ordnance," *IEEE Trans. Geosci. Remote Sens.*, vol. 39, no. 6, pp. 1221–1230, Jun. 2001.
[26] K. O'Neill, "Discrimination of UXO in soil using broadband polarimetric GPR backscatter," *IEEE Trans. Geosci. Remote Sens.*, vol. 39, no. 2, pp. 356–367, Feb. 2001.
[27] J.-S. Lee and E. Pottier, *Polarimetric Radar Imaging: From Basics to Applications*, 1st ed. Boca Raton, FL, USA: CRC, 2009.
[28] S. R. Cloude and E. Pottier, "An entropy based classification scheme for land applications of polarimetric SAR," *IEEE Trans. Geosci. Remote Sens.*, vol. 35, no. 1, pp. 68–78, Jan. 1997.
[29] E. Guillanton, J. Y. Dauvignac, C. Pichot, and J. Cashman, "A new design tapered slot antenna for ultra-wideband applications," *Microw. Opt. Technol. Lett.*, vol. 19, no. 4, pp. 286–289, Nov. 1998.
[30] M. Sato *et al.*, "GPR using an array antenna for landmine detection," *Near Surface Geophys.*, vol. 2, no. 1, pp. 7–13, Feb. 2004.

Xuan Feng (M'10) received the B.S. degree in applied geophysics and the M.S. and Ph.D. degrees in geo-exploration and information technology from Jilin University, Changchun, China, in 1996, 1999, and 2002, respectively.

From 2003 to 2005, he held a postdoctoral position, and from 2005 to 2006, he was a Research Assistant with Tohoku University, Sendai, Japan, respectively. From 2006 to 2008, he was an Associate Professor with Jilin University. Since 2008, he has been a Professor with Jilin University and has been the Director of the Geophysical Department since 2013. From 2014, he has also been a Visiting Scientist in the Earth Resources Laboratory, Department of Earth, Atmospheric and Planetary Sciences, Massachusetts Institute of Technology, Cambridge, MA, USA. His research interests include signal processing technology of ground penetrating radar (GPR) and seismic exploration, and joint inversion of GPR and seismic exploration.

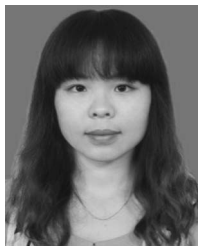

Yue Yu received the B.S. degree in physics from Jilin Normal University, Sipin, China, in 2011, where she is currently working toward the Ph.D. degree in geophysics in the College of Geo-Exploration Science and Technology, Jilin University, Changchun, China.

Her research interests include system and signal analysis of ground penetrating radar.

Cai Liu received the B.S. degree in applied geophysics and the M.S. and Ph.D. degrees in geo-exploration and information technology from Jilin University, Changchun, China, in 1986, 1993, and 1999, respectively.

From 1996 to 2000, he was an Associate Professor with Jilin University and became a Professor in 2000 and a Distinguished Professor of Jilin Province, China, in 2008. He has been the Director of the College of Geo-Exploration Science and Technology, Jilin University, since 2004. His research interest is the integrated research of geophysics and geology.

Michael Fehler received the B.A. degree in physics from Reed College, Portland, OR, USA, in 1974 and the Ph.D. degree in seismology from the Massachusetts Institute of Technology, Cambridge, MA, USA, in 1979.

From 1979 to 1984, he was an Assistant Professor of geophysics in the College of Oceanography at Oregon State University, Corvallis, OR, USA. He was at Los Alamos National Laboratory from 1984 to 2007 where he was the Group Leader of the Geophysics Group and later the Division Director of the Earth and Environmental Sciences Division. Since 2008, he has been a Senior Research Scientist in the Department of Earth, Atmospheric, and Planetary Sciences at the Massachusetts Institute of Technology. He was the Project Manager for the Phase I portion of the Society of Exploration Geophysicists Advanced Modeling (SEAM) project between 2007 and 2013. Since 2014, he has the Project Manager of a SEAM project that focuses on predrill pore pressure prediction. He coauthored a book, *Seismic Wave Propagation and Scattering in the Heterogeneous Earth* (Springer, 1997) and in 2012 coauthored a second edition of the same book.

Dr. Fehler was the Editor-in-Chief of the *Bulletin of the Seismological Society of America* for nine years beginning in 1995 and was the President of the Seismological Society of America from 2005 to 2007.